Title

Evolutionary optimization of the multidimensional parameter space governing tungsten oxidation in fusion environments

Journal

Nuclear Fusion, 66(7)

ISSN

0029-5515

Authors

Zhang, Siyu
Yu, Jinxin
Marian, Jaime

Publication Date

2026-07-01

DOI

10.1088/1741-4326/ae72a2

Peer reviewed

OPEN ACCESS
IOP Publishing | International Atomic Energy Agency Nuclear Fusion
Nucl. Fusion **66** (2026) 076014 (14pp) https://doi.org/10.1088/1741-4326/ae72a2

Evolutionary optimization of the multidimensional parameter space governing tungsten oxidation in fusion environments

Siyu Zhang, Jinxin Yu and Jaime Marian*

Department of Materials Science and Engineering, University of California Los Angeles, Los Angeles, CA 90095, United States of America

E-mail: jmarian@ucla.edu

Received 12 January 2026, revised 29 April 2026
Accepted for publication 26 May 2026
Published 9 June 2026

Abstract

Tungsten is a primary candidate for plasma-facing components in fusion devices, but its susceptibility to rapid oxidation during accidental air ingress poses significant safety risks. Existing models of tungsten oxidation often rely on individual parameters (such as oxygen diffusivity and adsorption energies) derived from first principles simulations, which frequently fall far from accurately explaining experimental oxidation rate trends. This study uses an improved multilayer interface tracking model that treats the oxide scale as a dynamic system of WO_3, $WO_{2.9}$, $WO_{2.72}$, and WO_2 layers. To address the unknown nature of many layer-specific parameters, we employ a Differential Evolution genetic algorithm to optimize a 13-dimensional parameter space against a comprehensive database of experimental growth constants. The resulting optimized model accurately reproduces experimental oxidation kinetics and correctly predicts the temperature-dependent evolution of specific oxide phases, providing a more reliable tool for assessing the performance of fusion materials under extreme conditions. The model can be dynamically improved by incorporating experimental data as they become available, leading to parameters that reflect the state of the art in oxidation measurements and characterization.

Keywords: tungsten, fusion materials, oxidation, modeling and simulation

(Some figures may appear in colour only in the online journal)

1. Introduction

Tungsten (W) has long been considered the leading candidate for plasma-facing components (PFCs) in magnetic fusion devices due to its low sputtering yield, high thermal conductivity, and minimal tritium retention under neutron irradiation [1–3]. These properties make W particularly suitable to be used as armor in divertors and first-wall structures [4–6]. Although PFC are designed to operate in vacuum conditions, accidental scenarios such as a during a loss of coolant (LOCA) or loss of integrity of the vacuum vessel can introduce oxidizing atmospheres [2] that can lead to the rapid oxidation of W and the formation of a highly-volatile tungsten oxide scale [7–9]. The observed structure of the oxide is generally consistent with the thermodynamic presence of a sequence of stable oxides ranging from WO_2 to WO_3, with the oxygen-deficient $WO_{2.9}$ and $WO_{2.72}$ in between them. Thermochemical and mechanical mismatches among these layers generate internal

* Author to whom any correspondence should be addressed.

stresses that promote cracking and spallation [9], while the high vapor pressure of WO_3 drives rapid mass loss through sublimation [7, 10].

Multiple studies have established that the rate-limiting process for the growth of the oxide scale is oxygen transport through the oxide(s). Indeed, the oxidation kinetics in tungsten is generally described using a parabolic dependence between the mass loss of metal and time [8, 9, 11–13], only broken when cracks and cavities form after a critical oxide scale width, where a transition to a linear law takes place [7, 9, 14]. While determining the value of the parabolic rate constant is important to quantify the time-dependent oxidation kinetics, an analysis based on total mass loss ignores the role played by the different oxide layers in the overall evolution, as has been recognized experimentally [7, 8, 10]. To capture the chemical complexity of fully-formed W oxide scales, a multilayer interface tracking model has recently been developed [15], from which the individual role played by each specific oxide structure can be studied to assess their effect on the value and temperature dependence of the parabolic rate constant $K_p(T)$. The model uses oxygen adsorption energies, oxygen diffusivities, and saturation solubilities in each of the oxide layers, most of which are unknown due to the difficulty in measuring oxygen anion energetics in experiments [12]. Density functional theory (DFT) has been used to calculate some of these parameters [15–18], but validation remains limited due to the lack of dedicated layer-dependent measurements. Additionally, caution should always be exercised when using DFT calculations obtained from unrealistically idealized material conditions, particularity in view of the highly-complex tungsten oxide microstructures observed experimentally. Indeed, predictions of K_p using the DFT-parameterized model showed significant discrepancies in both magnitude and temperature trend compared with experiments, particularly in the mid-temperature regime (873∼1273 K).

An alternative approach to work with under-determined multi-parametric physics models of chemical oxidation is to utilize genetic algorithms aimed at optimizing the global response of the model against an objective function defined by experimental data. Specifically, in this work we carry out a multidimensional optimization by evolutionary searches of the parameter space governing oxygen adsorption and diffusion in the different tungsten oxides. The search is initiated either with randomly-generated parameter sets or with the set obtained by Huang *et al* [15], and is performed within numerical boundaries that (i) are consistent with the physics of tungsten oxidation, and that (ii) narrow down the potentially infinite parameter range space, leading to significant convergence acceleration. Our approach considers the 13-dimensional set of model parameters (diffusion pre-factors, activation energies, and adsorption energies) and provides an optimized set that globally approximates the experimental measurements of $K_p(T)$ from the most extensive database compiled to date. We employ the *differential evolution* (DE) genetic algorithm [19–22], which is a stochastic, population-based evolutionary method designed for continuous global optimization. DE optimizes parameters by generating new candidate solutions using scaled differences of randomly chosen population members, mixing them with current solutions, and keeping only those that improve agreement with the objective function, causing the population to converge toward the global optimum.

2. Methods

2.1. Physical model of W oxidation

2.1.1. General description. Our physics model consists of a one-dimensional multilayer stack $WO_3/WO_{2.9}/WO_{2.72}/WO_2/W$ with moving interfaces $x = s_i(t)$ driven by oxygen fluxes [23]. The model adopts specific oxide stoichiometries for consistency with the W–O phase diagram in the relevant temperature range, namely, $WO_3, WO_{2.9}, WO_{2.72}$ and WO_2, all which are seen to behave as compounds with very narrow stability ranges in oxygen concentration. The model is an expanded version of that published in [15], and here we simply discuss the modifications undertaken in the present work.

The total oxygen concentration is partitioned between 'free' oxygen and 'chemical' oxygen. Free oxygen is mobile and diffuses within each phase in a thermally-activated fashion with diffusivities described by the general Arrhenius form: $D_\alpha(T) = D^0_\alpha \exp(-E^m_\alpha/k_B T)$, where D^0_α, E^m_α, and k_B are the pre-factor and migration energy in compound α, and Boltzmann's constant, respectively. For its part, chemical oxygen c_{ch} represents the oxygen fixed by a given oxide phase as they form, so that $c_{tot} = c_f + c_{ch}$. We impose phase-specific caps on c_{ch}, commensurate with the stoichiometry of each oxide, while for c_f we set limits for WO_2 and W, allowing for a discontinuity of mobile oxygen across WO_2/W while maintaining total oxygen mass conservation. The outermost surface takes up oxygen from the environment at a set rate. The W metal region is solved for explicitly, so that the evolving metal-side gradient provides the boundary condition at the WO_2/W interface. A schematic of layers and concentrations is shown in figure 1. Boundary conditions are summarized in table 1. Governing equations follow in sections 2.1.2 and 2.1.3.

2.1.2. Interface equation of motion. The motion of each interface is set by a mass balance: the interface advances or recedes according to the difference between the outgoing and incoming oxygen fluxes evaluated on the two sides of the boundary. We adopt the sign convention that J_i^+ is the flux *out of* the interface into the phase on the right side, and J_i^- is the flux *into* the interface from the phase on the left side. This leads to the Stefan equation at an interface *i*:

$$\dot{s}_i = \frac{J_i^+ - J_i^-}{n\,\rho_W} \tag{1}$$

where

$$J^\pm = -D\left.\frac{\partial c}{\partial x}\right|_{s^\pm}. \tag{2}$$

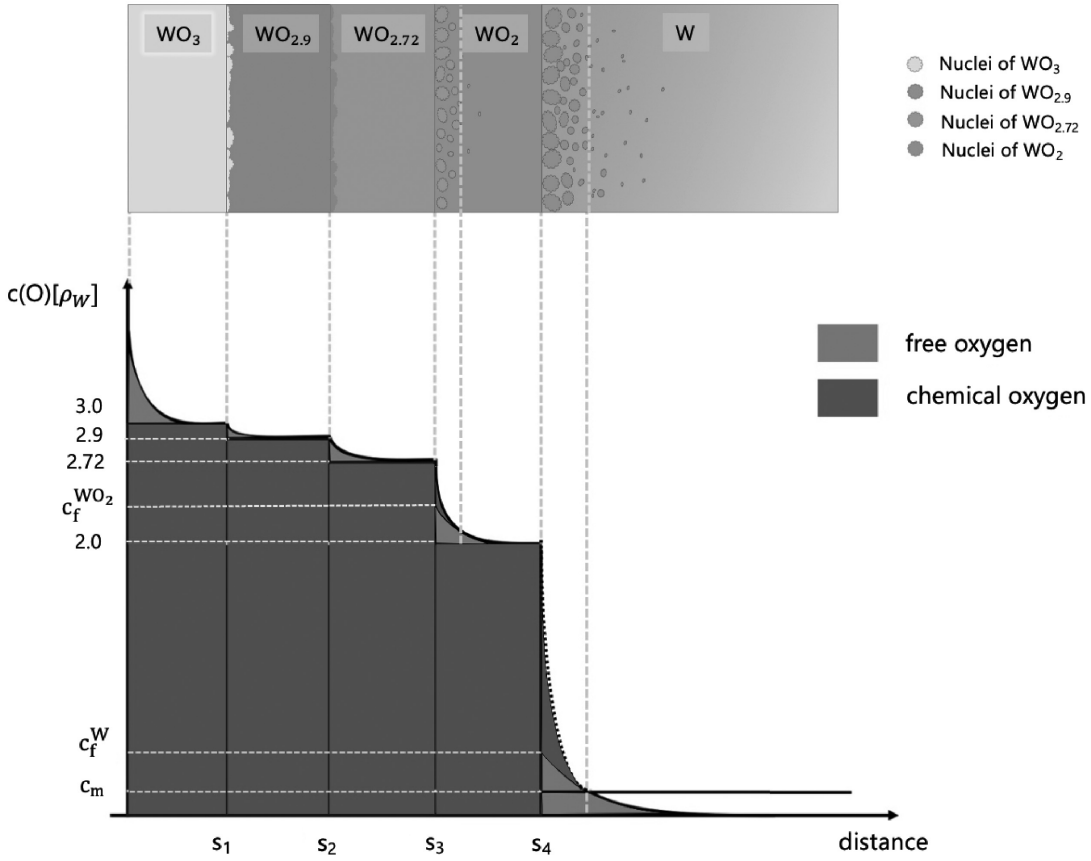

Figure 1. Schematic diagram of the multilayer oxide stack and oxygen partitioning. Orange regions denote free (mobile) oxygen and blue denotes chemical (bound) oxygen. Horizontal dashed lines indicate the maximum O concentration values of c_{f} for WO_2 and for W metal. Vertical dashed lines s_1–s_4 mark interfaces between WO_3, $WO_{2.9}$, $WO_{2.72}$, WO_2, and W.

The interface advances when $J_i^+ > J_i^-$ and recedes otherwise; this corresponds to the direction of the local chemical-potential drop across the boundary under the prevailing T and oxygen concentrations. Oxygen fluxes described by equation (2) are obtained by solving Fick's second law for each separate layer on a fine spatial mesh that sets the time scale of the problem according to standard numerical stability criteria. Details are provided in [15]. Layers are evolved in parallel and coupled only through their shared interfaces, from where the equations of motion are then integrated in time. The boundary conditions for all layers are provided in table 1. In the Stefan model, the motion of each interface is governed by the imbalance of oxygen fluxes across the boundary. These fluxes are driven by gradients in oxygen chemical potential, which control both the direction of interface motion and the selection of stable oxide phases. As a result, each oxide phase forms within a specific oxygen chemical potential window.

Because the metal layer is much thicker than the oxides, it requires a coarser spatial discretization, and its much higher oxygen diffusivity introduces distinct characteristic time and length scales. In this work, the metal layer refers to the unoxidized tungsten substrate adjacent to the oxide scale, where oxygen may be present only up to its temperature-dependent solubility limit. These factors together make direct coupling with the oxide layers numerically impractical, as they impose incompatible mesh resolutions in both space and time. To address this, the diffusion problem in W-metal is solved separately, and the oxygen concentration gradient near the WO_2/W interface is approximated by a smooth empirical function of time. This fitted expression provides a tractable representation of the W-side gradient, from which the outgoing flux is evaluated using Fick's first law:

$$J_4^+(t) = -D_{\mathrm{W}}(T)\left.\frac{\partial c}{\partial x}\right|_{x=s_4^+}.$$

The resulting flux is then applied as the dynamic boundary condition for the WO_2 region and enters the Stefan balance for the WO_2/W interface:

$$\dot{s}_4 = \frac{J_4^+(t) - J_4^-(t)}{2\rho_{\mathrm{W}}}.$$

This approach ensures that interface motion is governed by the evolving W-side concentration gradient arising from subsurface oxygen accumulation.

2.1.3. Surface uptake at the environment side. Oxygen from the environment adsorbs onto the surface and diffuses inward through the oxide layers. Each surface oxide α presents a distinct adsorption barrier, leading to different surface fluxes

Table 1. Boundary conditions for each layer. c denotes the free oxygen concentration expressed in units of fraction of tungsten atomic density, ρ_W. b is the fixed free-oxygen concentration at the outer boundary of the WO_2 layer, i.e. at $x = s_3$, representing the maximum concentration of free oxygen in the WO_2 phase. a is the fixed free-oxygen concentration imposed at the WO_2/W interface on the W-metal side, i.e. at $x = s_4$, indicating the maximum concentration of free oxygen in the W phase.

Layer	Compound	Outer interface	Inner interface	Outer boundary condition	Inner boundary condition
1	WO_3	$x = 0$	s_1	Surface uptake (equation (4))	$c = 0$
2	$WO_{2.9}$	s_1	s_2	$c = 0.1$	$c = 0$
3	$WO_{2.72}$	s_2	s_3	$c = 0.18$	$c = 0$
4	WO_2	s_3	s_4	$c = b$	Precomputed J^+_{int} in W
5	W	s_4	s_5	$c = a$	$J = 0$

as a function of the local oxygen concentration c_α depending on which oxide is exposed. The oxygen uptake rate displays thermally activated behavior:

$$\dot{c}^0_\alpha = c_0\,\nu^{\text{ads}}_\alpha(T) = c_0\nu^0_\alpha \exp\left(-\frac{E^{\text{ads}}_\alpha}{k_B T}\right) \tag{3}$$

where $\dot{c}_0$ is the intrinsic oxygen adsorption rate, c_0 is the ambient oxygen concentration (in principle dependent on the ambient oxygen partial pressure, but here taken as a constant value representative of standard atmospheric conditions [24]), ν^0_α is a transition attempt frequency, and E^{ads}_α is an effective absorption barrier governing the net oxygen incorporation rate[1]. The amount of oxygen that can be adsorbed by a given compound saturates at a maximum value, $c^{\max}_\alpha$, such that $\dot{c}^{\text{ads}}_\alpha = 0$ when $c = c^{\max}_\alpha$, i.e.:

$$\dot{c}^{\text{ads}}_\alpha = \left(\frac{c^{\max}_\alpha - c}{c^{\max}_\alpha}\right)\dot{c}^0_\alpha. \tag{4}$$

This form ensures that the adsorption rate decreases smoothly as the near-surface oxygen concentration approaches $c^{\max}_\alpha$ for a given oxide layer. For bulk oxides, we assume that all oxides saturate when roughly all interstitial sites in metallic W have been occupied, i.e.:

$$c^{\max}_{WO_2} = c^{\max}_{WO_{2.72}} = c^{\max}_{WO_3} \approx \rho_W.$$

2.1.4. Discontinuities in free oxygen profile and solubility limits. A modification in the present model with respect to the original one [15] is that the free oxygen concentration, c_f, is not required to be continuous across all interfaces. Discontinuities are permitted at the interfaces between oxide phases that display a region of phase coexistance in the phase diagram. Under such conditions, interfaces are not strictly sharp, but 'porous', indicating the presence of nuclei of the previous phase in the phase diagram in the new one. This gives rise to declining values of c_{ch}, see figure 1. To maintain mass conservation, the gap between the two adjacent stoichiometric compounds is closed by c_f. Because this gap changes across different interfaces and depends on the apparent width of each interface (i.e. the region over c_{ch} decays to zero), c_f displays jumps across each interface. This again is simply a reflection of the actual thermodynamics of the W–O system, which is more realistically captured in this fashion.

In this work, the width of each interface is set commensurately with the concentration range where two oxide phases may coexist.

2.2. Optimization parameter database

The model presented above provides a framework within which to simulate the time evolution of the multilayer W oxide system from the motion of individual interfaces. In the 'passivating' regime, i.e. when the oxide maintains structural integrity, the growth of each layer is governed by the diffusivity of oxygen, defined by the corresponding diffusion prefactors and migration energies. Consequently, the formation of each oxide layer occurs when the local oxygen concentration reaches the stoichiometric level required for the next oxide phase.

However, no experiments have been performed where the evolution of each interface has been characterized separately. Instead, so-called 'mass gain' experiments relate the growth of the whole oxide scale, without distinction of oxide type, to time by way of a parabolic growth law:

$$(\Delta m)^2 = K_p t \tag{5}$$

where K_p is the growth constant and t is the time. Thus, if one wants to use exclusively experimental data to optimize the model parameters, the procedure to be developed will be necessarily required to handle a reduction in dimensionality from coupled multilayer data to a single parameter K_p. The model is thus *under-determined* and, as discussed in section 1, the main objective of this paper is to map the physical parameters of the model to a series of experimental data of K_p so as to calibrate and validate individual diffusivity parameters for each layer. $\Delta m(t)$ is obtained in our model by adding the oxygen content across all oxide layers as:

$$\Delta m(t) = m_O \sum_i \int_{s_{i-1}}^{s_i} c^i_{ch}(x,t)\,\mathrm{d}x, \tag{6}$$

where m_O is the molar mass of oxygen and s_{i-1} and s_i are the bounds of a given oxide layer i. K_p is then extracted by fitting equation (5) to the square of $\Delta m(t)$ obtained from equation (6).

[1] We note that only a fraction of the chemisorbed oxygen contributes to bulk transport, and thus E^{ads}_α does not represent a pure adsorption energy.

Table 2. Model parameters for WO_3, $WO_{2.72}$, WO_2, and W. In parenthesis and black color, starting parameters based on existing model in [15]. In red color, optimized parameters after convergence following the procedure described in section 2.3.

Phase	D_0 ($m^2 \cdot s^{-1}$)	E_m (eV)	E_{ads} (eV)
WO_3	(6.8×10^{-6}) 8.06×10^{-6}	(1.30) 1.82	(1.0) 1.87
$WO_{2.72}$	(6.8×10^{-6}) 1.83×10^{-7}	(1.22) 2.07	(1.0) 2.01
WO_2	(3.1×10^{-5}) 3.26×10^{-7}	(1.90) 2.09	(1.0) 2.03
W	(7.6×10^{-8}) 8.00×10^{-3}	(0.15) 1.67	(1.7) 1.0
Other parameters			
c_W^{max}		$(2.0\rho_W)$ $0.056\rho_W$	
$c_{WO_2}^{max}$		$(2.72\rho_W)$ $2.56\rho_W$	

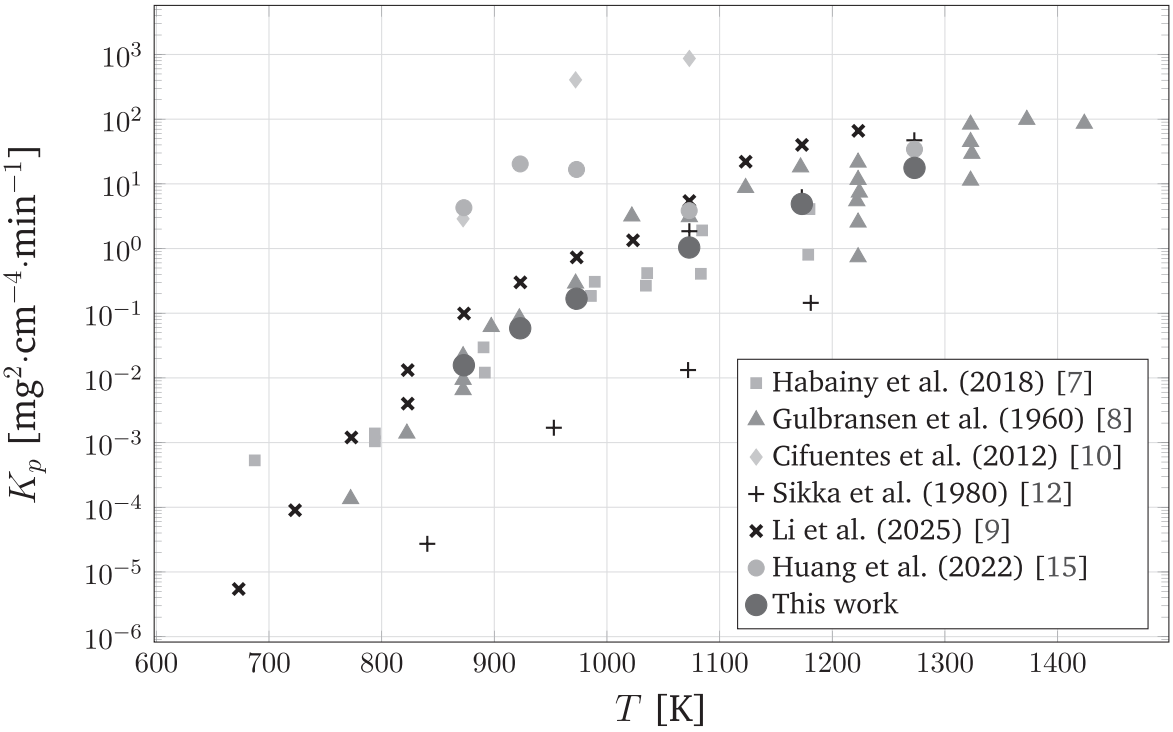

Figure 2. Comparison between simulated parabolic rate constants and experimental data from the literature.

Alternatively, one could use electronic structure calculations (the only approach where each oxide layer can be considered separately) to calculate the diffusion parameters. Here, the starting values for these coefficients are taken from the original model in [15] and are given in table 2 (in parenthesis).

2.2.1. Available experimental data. Figure 2 plots experimentally-measured values of K_p from several published sources as a function of temperature. Also plotted on the graph are the predictions based on our previous model using the parameters provided in table 2 [15]. Finally, the predictions generated by our data-driven approach (to be discussed below) are also shown.

2.2.2. Training database and information. The experimental data points presented in figure 2 are shown in figure 3 in an Arrhenius plot. A fit to the data using an Arrhenius expression, $K_p(T) = K_0 \exp(-\Delta Q/kT)$ yields $K_0 = 6.1 \times 10^7$ mg$^2 \cdot$ cm^{-4}·min^{-1} and $\Delta Q = 1.71$ eV. This ΔQ is in good agreement with recent experimental measurements yielding values of 1.87 [9] and 2.1 eV [11], respectively. The fitted expression for $K_p(T)$ is used as the global objective function from which the errors of the optimization approach will be calculated.

In addition, we use information extracted from post-oxidation characterizations to identify dominant and/or absent oxide phases at different temperatures to further inform our global optimization cycle. Table 3 lists the objective oxide layer stack based on cross-sectional analysis and qualitative layer color identification [8, 15]. The entry at 873 K has been revised to a ternary oxide stack, $WO_3/WO_{2.72}/WO_2$, instead of the originally reported dual structure $WO_{2.72}/WO_2$. While Gulbransen and Andrew [8] reported the presence of a WO_3 surface layer, Cifuentes *et al* [10] did not observe the tri-oxide

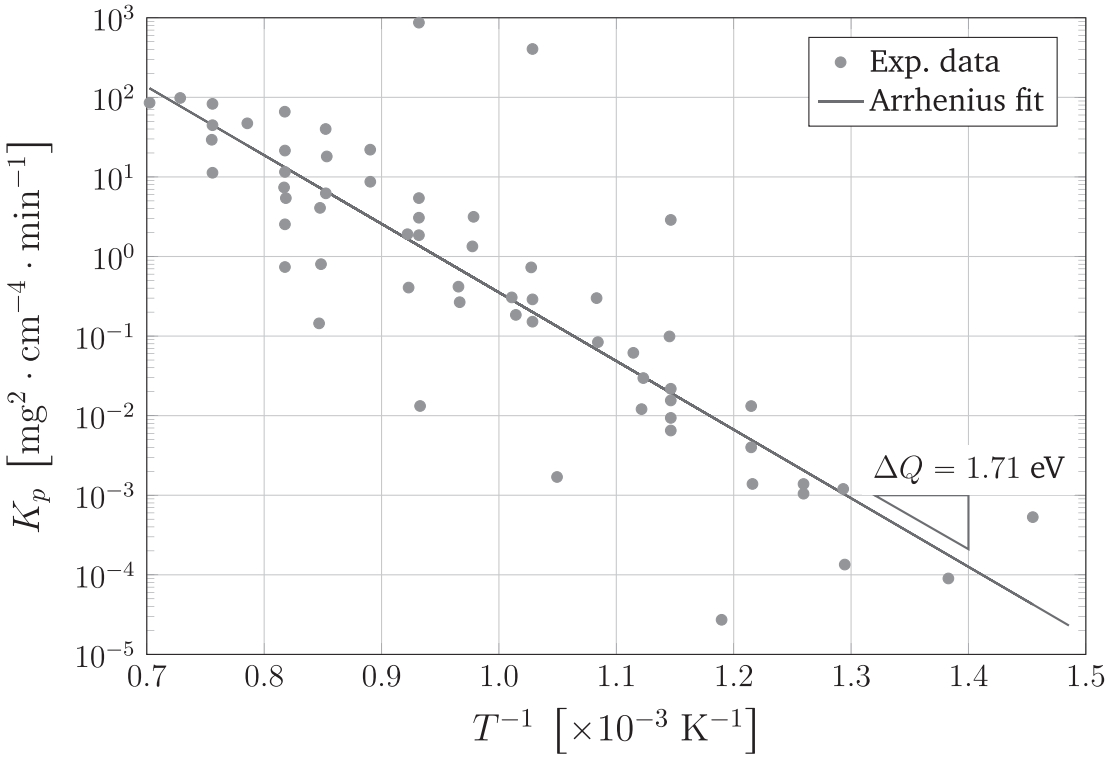

Figure 3. Arrhenius fit of the experimental data used in figure 2. The activation energy resulting from the fit, $\Delta Q = 1.71$ eV, is show for reference.

Table 3. Assigned oxide layer stacks as a function of temperature.

T (K)	Assigned oxide stack
873	$WO_3/WO_{2.72}/WO_2$
923	$WO_3/WO_{2.72}/WO_2$
973	$WO_{2.72}/WO_2$
1073	WO_2
1173	WO_2
1273	WO_2

within the first 360 min of oxidation. However, this could be due to slow kinetics resulting in a delayed formation of WO_3 within the time frame of some experimental tests. Indeed, DFT calculations indicate that $WO_{2.72}$ exhibits higher oxygen diffusivity than the adjacent oxide layers [15], which slows oxygen accumulation at the surface and could delay the nucleation of WO_3. This provides a natural explanation for why WO_3 is sometimes absent in some experiments but can eventually form on top of $WO_{2.72}$ once oxidation proceeds for sufficiently long times and the surface oxygen concentration surpasses the threshold of $2.9\,\rho_W$.

Similarly, for the entry at 1173 K, we have simplified the experimentally observed $WO_{2.72}/WO_2$ configuration to a single WO_2 layer to ensure consistency with neighboring temperature regimes. This simplification is considered justifiable as a result of the experimental difficulty in distinguishing oxide phases solely on the basis of color or visual contrast.

2.3. Parameter optimization approach

Our approach is based on an evolutionary optimization algorithm that modifies a set of *candidate* parameters through a series of generations aimed at minimizing a *loss function* $\mathcal{L}$, defined in section 2.3.1 below. The optimization strategy consists of a global search followed by a local refinement. Prior to both stages, the search bounds for each parameter are defined on the basis of available experimental measurements and empirical estimates. The global search, implemented using a *Differential Evolution* (DE) algorithm [20], explores the full parameter space to identify a near-optimal region, defined as the regime where the loss function no longer shows significant improvement over successive generations. Subsequently, a local optimization using the *Limited-memory* Broyden–Fletcher–Goldfarb–Shanno with bounds (L-BFGS-B) algorithm [25, 26] is performed to refine the solution in the neighborhood of the best candidate set obtained after the global search. The overall optimization workflow is illustrated in figure 4.

(i) Global optimization (DE):
DE is a stochastic, derivative-free, population-based algorithm that operates by evolving a population of candidate parameter sets through mutation, crossover, and selection, gradually minimizing the value of the loss function $\mathcal{L}$ over generations. We initialize the population by generating 100 s of random samples of the candidate parameter set within certain parameter bounds [27]. Alternatively, one

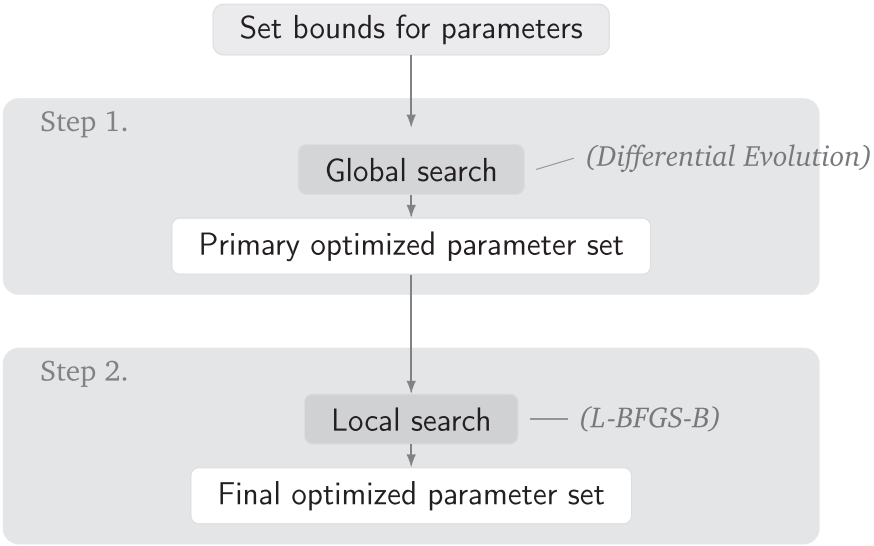

Figure 4. Two-step optimization workflow combining a global search (Differential Evolution with Best/1/bin mutation strategy) and a local refinement (L-BFGS-B).

can start from an existing parameter set (e.g. that in [15]) and either evaluate its suitability or use it to accelerate convergence. Here we try both types of initial conditions. For each generation g and target 13-dimensional vector $\vec{x}_i^{(g)}$, we apply a mutation strategy by which a mutant (donor) vector is formed by the operation equation (7):

$$\vec{v}_i^{(g)} = \vec{x}_{\text{best}}^{(g)} + F\left(\vec{x}_{r_1}^{(g)} - \vec{x}_{r_2}^{(g)}\right) \tag{7}$$

where the subindex i refers to different candidates within a given generation, F is a differential weight, and $\vec{x}_{\text{best}}$, $\vec{x}_{r_1}^{(g)}$, and $\vec{x}_{r_2}^{(g)}$ are three randomly-chosen candidates from the entire population. Of these three, $\vec{x}_{\text{best}}$ is the vector that yields the lowest value of $\mathcal{L}$. This vector undergoes binomial crossover with the target vector $\vec{x}_i^{(g)}$ to produce a trial vector $\vec{u}_i$, which inherits the 13 components from the mutant with probability p:

$$\vec{u}_i(q_j) = \begin{cases} \vec{v}_i(q_j), & \text{if } (\xi_j \leqslant p) \text{or } (j = n), \\ \vec{x}_i^{(g)}(q_j), & \text{otherwise,} \end{cases} \tag{8}$$

where j runs over all 13 components, q_j, of each vector, ξ_j is a random number in $(0:1]$, and m is a random number between 1 and 13. The loss function is evaluated for every candidate vector at each generation, and the approach selects the vector that leads to a lower value of $\mathcal{L}$:

$$\vec{x}_i^{(g+1)} = \min_{\vec{z} \in \left\{\vec{x}_i^{(g)}, \vec{u}_i\right\}} \mathcal{L}(\vec{z}). \tag{9}$$

Convergence is achieved when $\mathcal{L}$ shows no significant improvement over 30 consecutive generations. Specifically, we check whether the relative improvement falls below a small threshold ε:

$$\frac{\mathcal{L}_{\text{best}}^{(g-30)} - \mathcal{L}_{\text{best}}^{(g)}}{\max\left(1, \mathcal{L}_{\text{best}}^{(g)}\right)} < \varepsilon, \tag{10}$$

where ε is a prescribed tolerance (set to, e.g. 10^{-6}) that controls how strictly convergence is defined (small values of ε require sharper improvement, while larger values allow earlier termination). If this condition is not met, optimization continues until a maximum generation limit of 300 is reached. We fix $F = 0.5$ as a mid-range differential weight and $p = 0.5$ as a moderate crossover rate, both of which offer robust performance across a range of problem types.

(ii) Local polishing (L-BFGS-B):
Once the DE step converges, we perform a single local refinement using the L-BFGS-B algorithm, initialized at the best solution found by DE. L-BFGS-B is a quasi-Newton method that uses gradient information and supports box constraints, making it suitable for our bounded, differentiable objective. The polishing stage is run with a generous iteration limit ($\sim$1000) but strict tolerances ($\sim 10^{-12}$), ensuring that the optimizer fully converges to a nearby local minimum. We log the value of $\mathcal{L}$ at each iteration to monitor convergence and stop polishing once the gradient norm or relative loss change falls below the threshold. This single polishing step typically sharpens the fit and improves numerical stability without significantly increasing runtime.

2.3.1. Loss function formulation. In this work, the loss function $\mathcal{L}$ is defined as:

$$\mathcal{L} = P_{K_p} + P_{\text{mode}} + P_{873\text{K}}. \tag{11}$$

Each term contributing to $\mathcal{L}$ is described in detail next.

- P_{K_p}: For each temperature, the simulated parabolic rate constant $K_{p,\mathrm{sim}}$ is compared against the experimental value $K_{p,\mathrm{exp}}$. The discrepancy is measured as the squared difference in logarithmic scale:

$$P_{K_p} = \sum_i \left[\log_{10}\left(K_{p,\mathrm{sim}}^{(i)}\right) - \log_{10}\left(K_{p,\mathrm{exp}}^{(i)}\right)\right]^2.$$

  This term ensures that the kinetics of oxide growth are quantitatively reproduced.
- P_{mode}: In addition to the oxidation kinetics, the model captures which oxide appears on the outer surface at each temperature. A large penalty is added whenever the simulated oxide-layer configuration does not correspond to the experimentally-observed one (see table 3):

$$P_{\mathrm{mode}} = 10^8 N_{\mathrm{mis}}$$

  where N_{mis} is the number of instances where the simulated outer oxide layer does not match the experimentally-observed one. This enforces the correct representation of the observed oxide stack.
- $P_{873\mathrm{K}}$: Published reports indicate that neither WO_3 nor $WO_{2.9}$ nucleate within the first 360 min at 873 K [8, 10]. From a physical point of view, this can be interpreted as the surface oxygen concentration staying below the required threshold of $2.9\rho_{\mathrm{W}}$. To encode this kinetic constraint, we introduce a conditional penalty:

$$P_{873\mathrm{K}} = \begin{cases} 10^8, & \text{if } c(x=0) \geqslant 2.9\rho_{\mathrm{W}} \text{at } T = 873 \text{ K}, t = 360 \text{ min}, \\ 0, & \text{otherwise.} \end{cases}$$

  This prevents the model from predicting unrealistically early growth of high oxides at 873 K.

Overall, this $\mathcal{L}$ function balances quantitative agreement with experimental $K_p(T)$ values, qualitative fidelity to observed oxide sequences, and physically realistic incubation behavior. In doing so, it provides a meaningful and rigorous criterion for parameter optimization, ensuring that fitted models reproduce both the rate and the mode of tungsten oxidation across a broad temperature range. To determine the unknown parameters, the model is evaluated at six temperatures: 873, 923, 973, 1073, 1173, and 1273 K. At each temperature, we compute contributions to the total loss and then sum them across all cases.

2.3.2. Particular constraint for $WO_{2.9}$ parameters. While $WO_{2.9}$ does not appear as a stable phase in experiments within our temperature range, its parameter space still plays a critical role in the model. We express this information as an inverse constraint: any parameter set that predicts $WO_{2.9}$ growth is penalized. This allows us to explore feasible combinations of diffusivity and adsorption parameters that are consistent with the absence of this intermediate oxide. We then performed a brute-force grid search [28] to explore the relevant parameter space. The search varies the pre-exponential diffusivity factor D_0 from 10^{-6} to 10^{-2} $\mathrm{m^2 \cdot s^{-1}}$ (logarithmically spaced over 10 values), the migration energy E_m from 1.0 to 1.8 eV (10 values), and the surface adsorption barrier E_{ads} from 1.0 to 3.0 eV (five values). At each grid point, the full forward model is executed, and a dedicated loss function was evaluated. Specifically, the appearance of $WO_{2.9}$ was penalized according to

$$\mathcal{L}_{\mathrm{WO_{2.9}}} = 10^8 N_{\mathrm{WO_{2.9}}} \tag{12}$$

where $N_{\mathrm{WO_{2.9}}}$ is the number of temperatures at which $WO_{2.9}$ is seen to emerge in the simulation. Candidate parameter sets are then selected by requiring $\mathcal{L}_{\mathrm{WO_{2.9}}} = 0$, corresponding to the absence of $WO_{2.9}$ formation in the simulated results. This criterion ensures that only parameter sets consistent with experimental growth sequences are retained.

3. Results

3.1. Optimized parameters for tungsten oxides and metallic tungsten

Using the approach described in the previous section, we optimized the diffusivity, solubility, and surface exchange parameters for WO_3, $WO_{2.72}$, WO_2, and metallic W. The DE search proved to be an efficient method to explore the broad parameter space. Figure 5 shows the evolution of the total loss $\mathcal{L}$ during the DE optimization (the subsequent local polishing step fine-tuned the DE-derived solution) for a number of independent optimization runs. Two types of initial conditions were considered. For the first type, the initial parameter set was generated by randomly selecting values within fixed prescribed parameter bounds (labeled as '*Random initial conditions*' in the figure). The second type was created by assigning some random variability to the parameter set obtained by Huang *et al* [15]. As the figure shows, convergence strongly depends on initial condition, both in final value and in the total number of iterations needed to reach it. By definition, the solutions corresponding to each converged set are not statistically equivalent. They actually represent how the inherent randomness of the optimization approach can lead to non-optimal (but converged) parameter sets. The optimal solution is that corresponding to the lowest final value of the loss function (shown in dark gray in figure 5), which yields the final parameter set provided in table 2 (in red color) next to the starting set for comparison. The lowest value achieved for $\mathcal{L}$ was found to be 4.7×10^{-7}.

Figure 6 displays an Arrhenius plot of the optimized oxygen diffusivities for all the oxide layers captured by the model, together with the values calculated by Huang *et al* [15]. A general observation, to be elaborated on in section 4, is that the optimized parameters involve lower diffusion prefactors but larger migration energies, leading to overall lower diffusivities.

The strong dependence of the optimized oxygen diffusivities on oxide stoichiometry shown in figure 6 reflects the substantial differences in crystal structure, thermodynamic stability ranges, and vacancy concentrations among the tungsten oxide phases considered. Although direct experimental measurements of oxygen diffusivity for each individual oxide

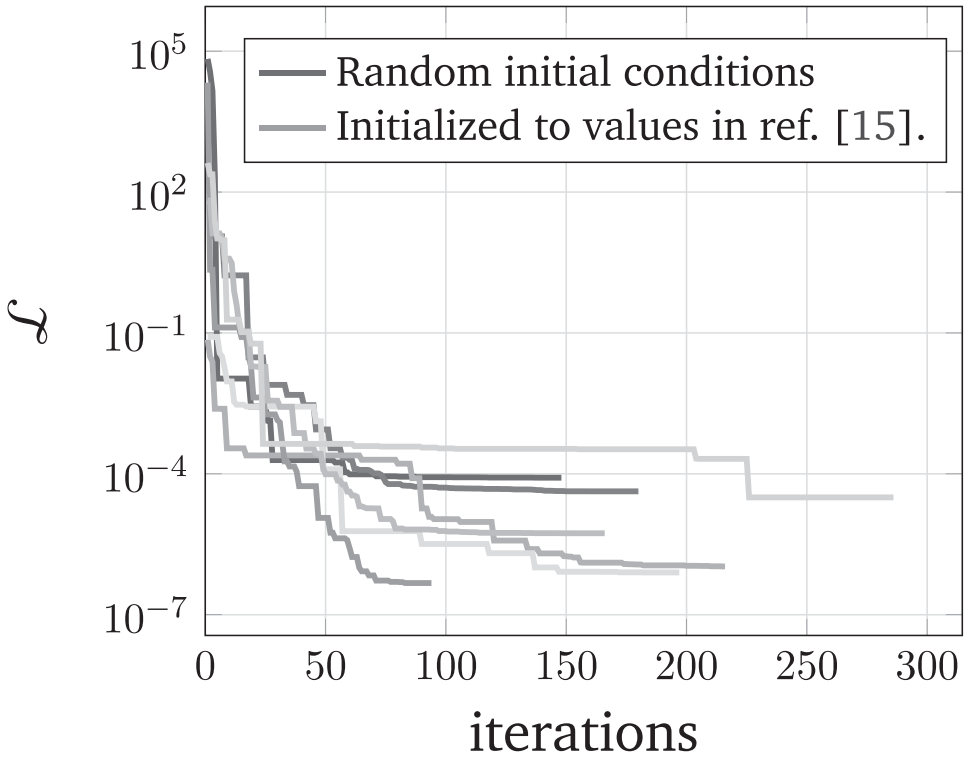

Figure 5. Evolution of the loss function $\mathcal{L}$ (defined in equation (11)) with the number of iterations (i.e. evolutionary optimization generations) for several different initial conditions.

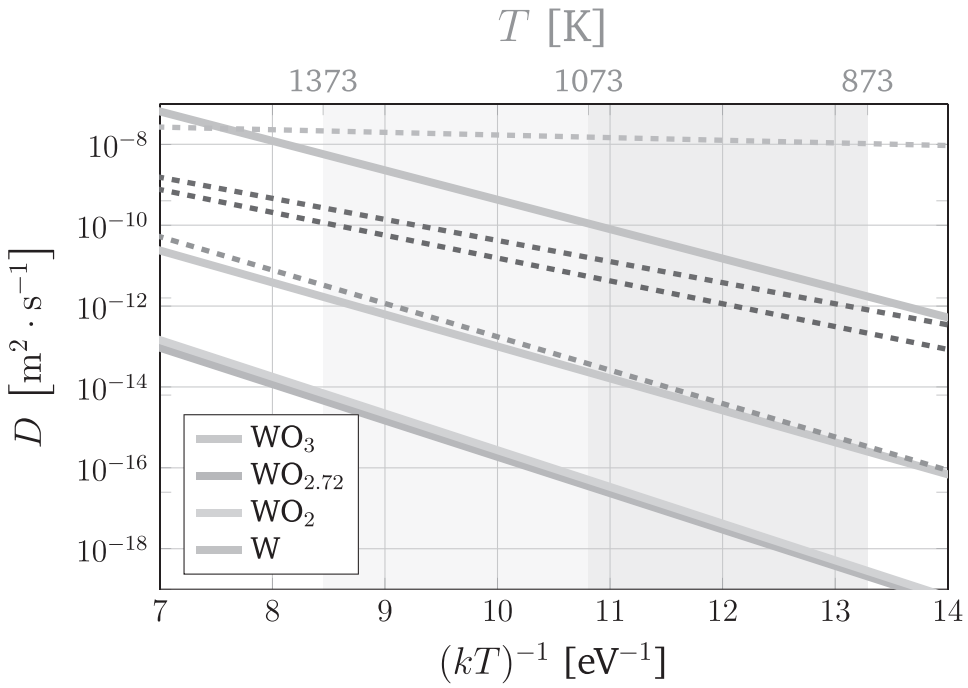

Figure 6. Arrhenius plot comparing the optimized oxygen diffusivities in this work (solid lines) with the calculated diffusivities from Huang *et al* [15]. Shaded regions mark the experimental temperature windows considered in this study: 873–1073 K (orange) and 1073–1373 K (gray).

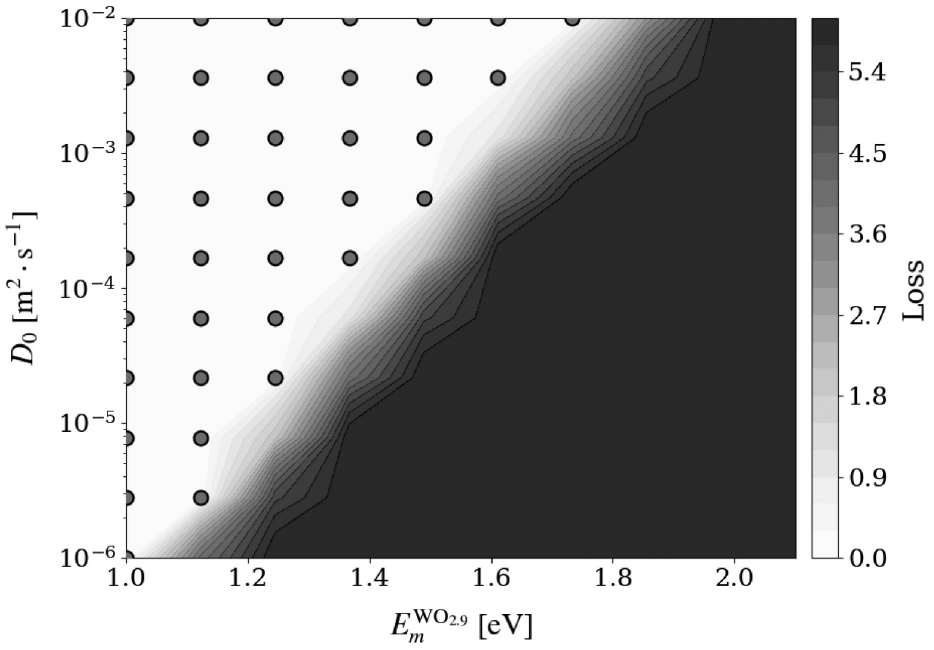

Figure 7. 2D contour slice of the $WO_{2.9}$ parameter landscape at $E_{ads} = 2.00$ eV. Stars mark the zero-loss (critical) parameter sets.

layer remain limited, the strong stoichiometry dependence is qualitatively consistent with experimental observations that different tungsten oxide phases exhibit markedly different properties.

3.2. Parameter constraints for $WO_{2.9}$

As mentioned above, $WO_{2.9}$ is not seen to appear as a standalone layer in any of the experiments of W oxidation (or, at best, it is folded generically with the WO_3 layer). To further investigate the role of $WO_{2.9}$ in the multilayer oxidation sequence, we carried out a three-way study were we analyzed jointly the effect of the oxygen adsorption energy, the diffusion pre-factpr, and the migration energy of oxygen in $WO_{2.9}$. To that end, we performed a brute-force grid search over the following parameter ranges:

- $10^{-6} < D_0^{WO_{2.9}} < 10^{-2}$ $[m^2\cdot s^{-1}]$
- $1.0 < E_m^{WO_{2.9}} < 1.8$ [eV]
- $1.0 < E_{ads}^{WO_{2.9}} < 3.0$ [eV].

The first result from this study is that $D_0^{WO_{2.9}}$ and $E_m^{WO_{2.9}}$ are completely insensitive to the value of $E_{ads}^{WO_{2.9}}$. Figure 7 shows the values of $\left(D_0^{WO_{2.9}}, E_m^{WO_{2.9}}\right)$ pairs that yield values of the loss function within the allowed tolerance (red dots), and the range for which the loss function failed to converge below (dark-shaded region). This confirms that the behavior of $WO_{2.9}$ is controlled by the oxygen diffusivity, with surface exchange playing a secondary role.

From the figure, a numerical expression linking the allowable pairs of the diffusivity prefactor and migration energy is:

$$E_m \lesssim 0.15 \log_{10}(D_0) + 1.90 \qquad (13)$$

Table 4. Fitted parameters a and b in the $s_4(t) = at^b$ power laws at different temperatures.

T (K)	a (μm $\cdot$ min^{-b})	b
873	0.13	0.62
973	0.92	0.55
1073	2.80	0.52
1173	6.09	0.52
1273	11.68	0.52

i.e. when D_0 and E_m satisfy this inequality, the model reproduces the correct growth mode and parabolic rate constants. This condition can therefore be viewed as a *subdimensional* Pareto front for the effective diffusion parameters of $WO_{2.9}$ within the multilayer oxidation framework.

The complete set of optimized parameters is then used to run the multilayer model as a function of temperature and the values of the rate constant K_p^{sim} are extracted according to equations (5) and (6). The results for K_p^{sim} are given are shown as red circles in figure 2. As it can be seen, the optimized rate constants display a more robust agreement with experimental data over the nearly five orders of magnitude in temperature considered here.

3.3. Time evolution laws for oxide layers

Under oxygen diffusion-controlled conditions, the growth of a single oxide layer is always expected to evolve under a parabolic time law (see equation (5)). However, with multiple oxide layers in coexistence, as is the case here, each with its own oxygen diffusivity and in a wide temperature range, it is worth testing whether the quadratic scaling still holds. To

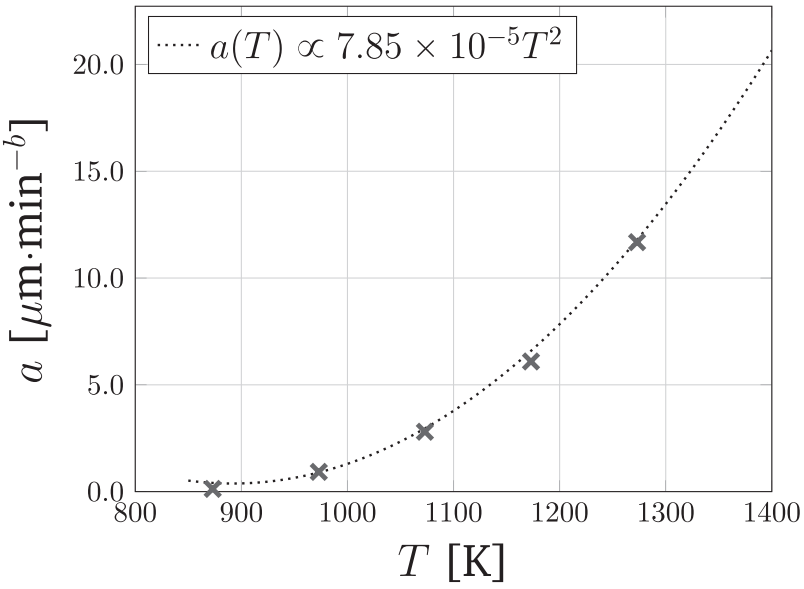

Figure 8. Temperature dependence of the parameter a in the expression $s_4(t) = at^b$. A polynomial fit to the data is provided, with the leading term of the fit shown in the legend. Values for b can be found in table 4.

that end, we used optimized diffusivity parameters to simulate the time of evolution of the entire oxide stack and then track the position of the innermost oxide surface (WO_2/W metal interface, s_4 in figure 1) and fit the resulting s_4-t curves to a power law of the type: $s_4(t) = at^b$. Table 4 shows the results of the fitting, with high temperatures clearly displaying quadratic behavior, but some deviations from pure diffusive kinetics (i.e. $b = 0.5$) being observed below 973 K, and particularly at 873 K

Interestingly, the parameter a itself appears to display a quadratic dependence on temperature, as illustrated in figure 8. Values of a are expressed in units of $\mu\text{m} \cdot \text{min}^{-b}$ for the values for b given in table 4. A polynomial fit to the data results in:

$$a(T) = 7.85 \times 10^{-5} T^2 - 0.14T + 62.8. \qquad (14)$$

The above expression is valid only while the oxide layer maintains its mechanical integrity. Once it reaches a critical thickness, epitaxial stresses can lead to the development of porosity or spall fracture of the oxide, which fragments into highly volatile dust [29, 30]. This typically happens at thicknesses below 10 microns.

4. Discussion

Tungsten oxidation is notoriously difficult to model because it involves the formation of an oxide 'stack', i.e. a multilayer sequence of different oxides each with its own separate physical properties. Our study is aimed at using all the available published experimental data on W oxidation—obtained over different decades, with different instrumentation, and under different conditions–, to extract an optimal set of oxygen diffusion parameters that would otherwise be very difficult to determine. Further, our approach has the built-in flexibility to take in new experimental data as they become available, allowing for the refinement of the optimal parameter sets in a dynamic fashion.

A crucial aspect of this work is the definition of the loss function, whose choice ultimately determines the quality and accuracy of our predictions. For this purpose, it is essential to possess a solid understanding of atomic diffusion processes, perform a careful interpretation of literature results, and know and understand the potential applications of the methods to be developed, all things that current independent agents powered by artificial intelligence cannot yet do. As well, we have shown that the initial parameter set can constrain the downstream convergence of the optimal set. For that reason, it is important to add variability in the initial conditions to remove any undue influence of the initial set and appropriately sample the optimization pathways.

While the optimization approach presented here is not intended as a replacement of DFT calculations, analyzing the discrepancies between both methods can help identify gaps in our theoretical understanding of oxygen diffusion in W oxides, or to recognize the large differences between small ideal computational supercells and real oxide lattices. More importantly, our work can help provide an experimentally-supported numerical tool to perform rapid calculations of W oxidation under a variety of conditions with the assurance of relevance in real oxidation scenarios. Although the model is not intended to replace experimental investigations, it can help extrapolate oxidation behavior to regimes where experimental data are scarce and guide the design of new experiments or oxidation-resistant tungsten-based materials relevant to PFCs in fusion reactors. Next, we discuss some specific aspects of the work that have implications for W as a PFC in fusion environments.

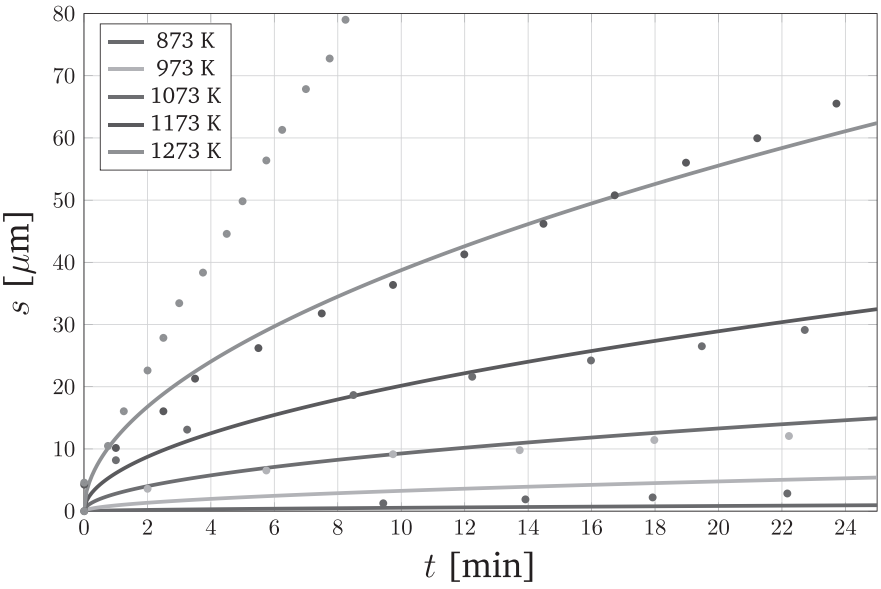

Figure 9. Comparison between model predictions based on equation (15) and experimental measurements extracted from [9].

4.1. Comparison of optimized oxide diffusivities with experiments and DFT calculations

Unlike metallic W, for which multiple experimental studies exist despite a relatively large value scatter, diffusivity measurements for tungsten oxides are almost nonexistent. The only direct measurement we are aware of is by Sikka and Rosa [12], who studied oxidation of non-stoichiometric WO_{3-x} (tungsten trioxide is often oxygen-deficient under atmospheric conditions), reporting values of $D_0 \approx 6.8 \times 10^{-7}$ $m^2 \cdot s^{-1}$ and $E_m \approx 1.29$ eV for oxygen-ion diffusion. These values reasonably close to our optimized values of $D_0 = 8.1 \times 10^{-6}$ $m^2 \cdot s^{-1}$ and $E_m = 1.82$ eV for WO_3 (see table 2). High-temperature permeation measurements using sealed tungsten capsules containing tungsten oxide provide permeation coefficients and activation energies for oxygen transport through the W/WO_x system [31]. While these data are reported as oxygen permeation through tungsten, the analysis explicitly involves equilibrium with tungsten oxides and thus reflects oxygen diffusion across tungsten-oxide layers above 2000 °C. Aitken *et al* [31] report a permeation energy of 1.73 eV, in good agreement with our value of 1.87 eV for oxygen diffusion in WO_3.

Because of the general lack of experimental data, calculations of oxygen diffusion in tungsten oxide have been performed in recent years. Le *et al* [16] have performed one of the most detailed DFT investigations of oxygen diffusion in WO_3, explicitly mapping oxygen-vacancy migration pathways to identify the activated state and calculate the energy barriers. They reported migration energies ranging from 0.14 to 1.07 eV, depending on oxygen deficiency and migration direction in $WO_{2.9}$–$WO_{2.72}$. However, since diffusivity prefactors (D_0) were not reported, their results cannot be converted into full Arrhenius diffusivities or compared directly with our fitted data in figure 6.

A complementary DFT study was conducted by Huang *et al* [15], who calculated oxygen-vacancy migration barriers using small oxide supercells of WO_3, $WO_{2.9}$, and WO_2. They reported E_m values of roughly 1.2∼1.9 eV for oxygen migration in WO_3, $WO_{2.72}$, $WO_{2.9}$, and WO_2, corresponding to intrinsic vacancy migration within idealized lattice environments. These activation energies therefore reflect atomistic diffusion processes in idealized conditions, rather than macroscopic transport through realistic oxide scales. In the present model, oxygen migration in tungsten oxides is assumed to proceed via a vacancy-mediated mechanism, irrespective of stoichiometry, while in metallic W it is treated as interstitial diffusion. This description is consistent with the current understanding in the literature and is also adopted in DFT calculations [32, 33].

As shown in figure 6, the DFT-calculated diffusivities of Huang *et al* are between one and two orders of magnitude higher than those obtained in this work in the 700 to 1500 K temperature range. We interpret this systematic deviation as reflecting the inherent differences between idealized atomic diffusion derived from conventional DFT calculations and effective transport through real oxide scales obtained from the present oxidation model optimization. DFT studies typically evaluate oxygen migration through vacancy diffusion in idealized crystal structures, whereas the present model describes oxygen transport through real oxide scales, which are polycrystalline, stressed, and contain extended defects that hinder long-range oxygen migration. Accordingly, the diffusivities fitted here should be understood as effective transport coefficients under real oxidation conditions, whereas the DFT calculations are only able to capture the intrinsic oxygen-ion kinetics in perfect lattices. Together with the microscopic migration data from Le *et al*, our results provide a consistent multiscale framework linking atomistic defect motion to macroscopic oxidation kinetics in tungsten oxides.

4.2. Comparison of oxide adsorption energy barriers with previous studies

Estimates of the adsorption energy of oxygen ions on W surfaces place it between 0.25 and 4.0 eV depending on the surface orientation [34–37]. In contrast, experimental information on oxygen adsorption barriers for tungsten oxides is extremely limited, and no reliable quantitative values are available. Most estimates come instead from atomistic modeling. For example, Jin *et al* [38] investigated CO oxidation on WO_3(001) and found that O_2 adsorption is thermodynamically unfavorable on ideal stoichiometric surfaces (-0.4 eV) but becomes markedly stronger on oxygen-vacancy sites (1.1 eV). These findings indicate that adsorption energies on WO_3 surfaces vary considerably with local structure, generally spanning from sub-eV levels up to about 1 eV depending on defect concentration and surface orientation.

The adsorption barriers obtained in this work fall moderately above that range, with final values of 1.87 eV for WO_3, 2.01 eV for $WO_{2.72}$, and 2.03 eV for WO_2 (table 2). Given that our E_{ads} values represent effective kinetic parameters averaged over multiple surface orientations and oxidation stages, rather than single-site thermodynamic adsorption energies, they are reasonably consistent with the upper bound of the reported DFT trends.

4.3. Applicability of numerical results

Ultimately, our model is designed to predict the growth of the W oxide scale of fusion-grade W metal exposed to air at high temperature. These are conditions only to be expected during loss of vacuum or loss of integrity of the fusion reaction chamber, i.e. conditions to be avoided altogether except during accident scenarios. Anticipating the time-to-failure of the oxide layer can be useful to predict the moment of release of tungsten oxide dust into the environment. The growth of the full W oxide stack can be calculated using the final expression $s(t;T) = a(T)t^b$ combined from equation (14) and the values of b in table 4:

$$s\,(T;t) \approx \left(7.85\times10^{-5}T^2 - 0.14T + 62.8\right) t^{\,b\approx\begin{cases}0.5,\ T>1000\ \text{K}\\ 0.6,\ T<1000\ \text{K}\end{cases}} \tag{15}$$

which gives the thickness in microns when the time is expressed in seconds. Figure 9 shows a comparison of predictions based on equation (15) with the measurements by Li *et al* [9].

While the general functional form of expression (15) captures the trend of the experimental data quite well, the quantitative discrepancies observed between the model and the data are consistent with the differences in the predicted-vs-measured values of K_P shown in figure 2 (by a factor of 2∼5). As presented, our model uses a wide dataset and is not designed to provide a match to any specific subset. In this work we do not discriminate based on the quality of the different data subsets. However, given the wide variety in data origin, one could add different weights to certain experimental data over others and make the model reflect data quality in a user-specific way.

It should be noted that the present model focuses on oxidation in dry air conditions. In humid environments, the formation of hydroxide radicals may alter the oxygen transport behavior within the oxide scale and thus affect the overall oxidation kinetics. Experimental studies have reported significant differences between dry and humid oxidation of tungsten, highlighting the important role of water vapor in modifying oxidation behavior. Accounting for these processes would require additional mechanisms beyond those considered in the present work and would increase the complexity of the model. Nevertheless, extending the present framework to humid or steam oxidation conditions represents an important direction for future work, particularly in view of their relevance to realistic fusion accident scenarios [39–41].

5. Conclusions

We finish the paper with our most important summary points and conclusions.

(i) Successful integration of physics and data: The study demonstrates that combining a multilayer sharp-interface model with evolutionary optimization can bridge the gap between idealized atomistic calculations and complex experimental observations.

(ii) Robust optimization workflow: The two-step approach—using a global DE search followed by a local refinement—proved highly effective at identifying a global optimum in a complex, under-determined parameter space. The optimization outcomes display a dependence on the initial parameter set, which points at the need to consider an adequate mix of initial conditions to ensure convergenve to global optima.

(iii) Identified kinetic discrepancies: Optimized parameters reveal that oxygen diffusivities in tungsten oxides generally have lower pre-factors but higher migration energies than previously predicted by theoretical DFT models.

(iv) Refinement of oxide phase evolution: The model successfully captures the 'incubation' kinetics of higher oxides, such as WO_3, explaining why certain layers may be absent in short-term experimental tests but appear during prolonged oxidation. Through a specialized grid search and penalty-based optimization, we identify parameter ranges for $WO_{2.9}$ that are physically consistent with its observed absence as a standalone stable layer in most experiments.

Acknowledgments

The authors acknowledge financial support from the U.S. Department of Energy, Office of Fusion Energy Sciences (DOE-FES) under Contract DE-SC0018410. This work used computational and storage services associated with the Hoffman2 Cluster which is operated by the UCLA Office of Advanced Research Computing's Research Technology Group. This research used resources of the National Energy

Research Scientific Computing Center (NERSC), a DOE User Facility using NERSC Award DDR-ERCAP-0034805.

ORCID iDs

Siyu Zhang 0009-0004-5166-5632
Jaime Marian 0000-0001-9000-3405

References

[1] Zheng Z., Lai C., Zhou W., Wang Y., Zhang Y. and Wang J. 2023 *Materials* **17** 102
[2] Pintsuk G. 2012 Tungsten as a plasma-facing material *Comprehensive Nuclear Materials*, ed R.J.M. Konings (Elsevier) pp 551–81
[3] Howard L., Parker G.D. and Yu X.Y. 2024 *Materials* **17** 2104
[4] Mitteau R., Diez M. and Firdaouss M. 2024 *Nucl. Mater. Energy* **41** 101777
[5] Müller A.v., Schlick G., Neu R., Anstätt C., Klimkait T., Lee J., Pascher B., Schmitt M. and Seidel C. 2019 *Nucl. Mater. Energy* **19** 184–8
[6] Kporha F., Nordlund K. and Granberg F. 2025 *J. Nucl. Mater.* **613** 155856
[7] Habainy J., Iyengar S., Surreddi K.B., Lee Y. and Dai Y. 2018 *J. Nucl. Mater.* **506** 26–34
[8] Gulbransen E.A. and Andrew K.F. 1960 *J. Electrochem. Soc.* **107** 619
[9] Li R., Alvarez G., Ipakchi A., Cupertino-Malheiros L., Gilbert M.R., Martinez-Paneda E. and Prestat E. 2025 *Nucl. Mater. Energy* **45** 101988
[10] Cifuentes S.C., Monge M.A. and Perez P. 2012 *Corros. Sci.* **57** 114–21
[11] Nagy D. and Humphry-Baker S.A. 2022 *Scr. Mater.* **209** 114373
[12] Sikka V.K. and Rosa C.J. 1980 *Corros. Sci.* **20** 1201–19
[13] Abernethy R. 2017 *Mater. Sci. Technol.* **33** 388–99
[14] Reyes M., Aryanfar A., Baek S.W. and Marian J. 2018 *J. Nucl. Mater.* **509** 550–65
[15] Huang S., Kerr R., Murphy S., Gilbert M.R. and Marian J. 2022 *Modelling Simul. Mater. Sci. Eng.* **30** 085015
[16] Le H.M., Vu N.H. and Phan B.T. 2014 *Comput. Mater. Sci.* **90** 171–6
[17] Zhao Y., Dezerald L. and Marian J. 2019 *Metals* **9** 252
[18] Kerr R.D., Gilbert M.R. and Murphy S.T. 2025 *Comput. Mater. Sci.* **252** 113781
[19] Qin A.K., Huang V.L. and Suganthan P.N. 2008 *IEEE Trans. Evol. Comput.* **13** 398–417
[20] Jin H. and Liu M. 2009 An improved differential evolution algorithm for optimization *2009 IITA Int. Conf. on Control, Automation and Systems Engineering* pp 659–62
[21] Mehmood F., Pachter R., Murphy N.R., Johnson W.E. and Ramana C.V. 2016 *J. Appl. Phys.* **120** 233105
[22] Deng W., Shang S., Cai X., Zhao H., Song Y. and Xu J. 2021 Soft computing-a fusion of foundations *Methodologies Appl.* **25** 5277–98
[23] Optasanu V., Raceanu L. and Montesin T. 2012 Simulation of metal/oxide interface mobility: effects of mechanical stresses on geometrical singularities *Defect and Diffusion Forum* vol 323 (Trans Tech Publications) pp 109–14
[24] Engineering ToolBox 2001 Engineering toolbox 2002 (available at: www.engineeringtoolbox.com)
[25] Liu D.C. and Nocedal J. 1989 *Math. Program.* **45** 503–28
[26] The L-BFGS-B algorithm (available at: https://sepwww.stanford.edu/data/media/public/docs/sep117/antoine1/paper_html/node6.html) (Accessed 16 October 2025)
[27] Saad A., Engelbrecht A.P. and Khan S.A. 2024 *Appl. Sci.* **14** 9976
[28] Bergstra J. and Bengio Y. 2012 *J. Mach.: Learn. Res.* **13** 281–305
[29] Litnovsky A. *et al* 2017 *Phys. Scr.* **2017** 014012
[30] Reuban A., Chen J., Povstugar I., Litnovsky A., Coenen J.W., Linsmeier C. and Gonzalez-Julian J. 2024 *Materials* **17** 5749
[31] Aitken E., Conn P., Duderstadt E. and Fryxell R. 1966 General Electric Co. (NASA CR-54918)
[32] Yang L. and Wirth B.D. 2024 *J. Appl. Phys.* **135** 085109
[33] Kong X.S., Wu X., You Y.W., Liu C.S., Fang Q.F., Chen J.L., Luo G.N. and Wang Z. 2014 *Acta Mater.* **66** 172–83
[34] Gomer R. and Hulm J. 1957 *J. Chem. Phys.* **27** 1363–76
[35] Singleton J. 1967 *J. Chem. Phys.* **47** 73–82
[36] McCarroll B. 1967 *J. Chem. Phys.* **46** 863–9
[37] Kohrt C. and Gomer R. 1970 *J. Chem. Phys.* **52** 3283–94
[38] Jin H., Zhou H. and Zhang Y. 2017 *Sensors* **17** 1898
[39] Smolik G.R. 1992 Tungsten alloy oxidation behavior in air and steam: fusion safety program/activation products task *Technical Report* EGG-FSP-10166 (EG&G Idaho, Inc. Idaho Falls, ID (United States))
[40] Smolik G., Pawelko R., Anderl R. and Petti D. 2001 *Fusion Eng. Des.* **54** 583–91
[41] Greene G. and Finfrock C. 2002 *Exp. Therm. Fluid Sci.* **26** 917–29